

## Article

# Influence of Axial Installation Deviation on the Hydraulic Axial Force of the 1000 MW Francis Runner in the Rated Operating Condition

Yongsheng Liu <sup>1</sup>, Chengming Liu <sup>2</sup> , Yongsheng Zhang <sup>1</sup>, Xingxing Huang <sup>3</sup> , Tao Guo <sup>1</sup>, Lingjiu Zhou <sup>2</sup> and Zhengwei Wang <sup>4,\*</sup> 

<sup>1</sup> Sinohydro Engineering Bureau 4 Co., Ltd., Chengdu 610031, China

<sup>2</sup> College of Water Resources and Civil Engineering, China Agricultural University, Beijing 100083, China

<sup>3</sup> S.C.I. Energy, Future Energy Research Institute, Seidengasse 17, 8706 Zurich, Switzerland

<sup>4</sup> State Key Laboratory of Hydrosience and Engineering, Department of Energy and Power Engineering, Tsinghua University, Beijing 100084, China

\* Correspondence: wzw@mail.tsinghua.edu.cn

**Abstract:** To study the influence of the axial installation deviation of the runner on the hydraulic axial force of the 1000 MW Francis turbine unit, geometric models of the full flow passage of the Francis turbine with the runner sinking in the axial direction by 0, 0.5, 1, 1.5, 2.5, 4, and 5.5 mm were established. The geometric models of the upper crown clearance, lower band clearance, and pressure balance pipes were also built. The SST turbulence model was used in the CFD setup to numerically simulate the flow in the Francis turbine with different runner installation sinking values. The results show that the hydraulic axial force on the inner surface of the runner remains stable when the runner is lowered. The hydraulic axial force on the entire runner surface and the outer surface of the lower band decreases, and the hydraulic axial force on the outer surface of the upper crown clearance increases. All of these hydraulic axial forces gradually tend to stabilize as the amount descending from the runner increases. To study the reasons for the changes in hydraulic axial forces, the streamlines and fluid fields of different sections in the flow passage were analyzed in detail. It was found that periodic changes of vortices were generated in the clearance due to the influences of the geometric shape and wall rotation. These vortices affect the distribution of velocity and pressure and, thus, determine the hydraulic axial forces. The runner axial installation deviation has little influence on the streamlines, pressure, and velocity distribution in each flow passage, and only changes the velocity and pressure in the upper crown clearance and lower band clearance. Therefore, the axial installation deviation of the runner has a great effect on the hydraulic axial force on the outer surface of the upper crown and lower band and has a smaller impact on the runner passage and the hydraulic axial force on the inner surface of the runner. The conclusions in this study can be adopted as references for the installation accuracy control of other hydraulic Francis turbine units.

**Keywords:** 1000 MW Francis turbine; axial installation deviation; hydraulic axial force; CFD; vortex; clearance flow; installation accuracy control



**Citation:** Liu, Y.; Liu, C.; Zhang, Y.; Huang, X.; Guo, T.; Zhou, L.; Wang, Z. Influence of Axial Installation Deviation on the Hydraulic Axial Force of the 1000 MW Francis Runner in the Rated Operating Condition. *Energies* **2023**, *16*, 1878. <https://doi.org/10.3390/en16041878>

Academic Editor: Christopher Micallef

Received: 5 January 2023

Revised: 30 January 2023

Accepted: 1 February 2023

Published: 14 February 2023



**Copyright:** © 2023 by the authors. Licensee MDPI, Basel, Switzerland. This article is an open access article distributed under the terms and conditions of the Creative Commons Attribution (CC BY) license (<https://creativecommons.org/licenses/by/4.0/>).

## 1. Introduction

To date, hydropower has a history of more than 100 years and becomes a major component of the power industry. It promotes the process of social history and makes great contributions to the progress of world civilization. As the production front of the power system, hydropower station plays an important role in the environment of large-scale development and use of electricity. In recent years, China's achievements and experience in hydropower development have been highly and widely praised by the international community. The construction of large and medium-sized hydropower stations alleviates the employment pressure in the surrounding areas, and increases infrastructure construction

such as transportation. Moreover, it greatly improves the financial revenues of local governments and the power generation capacities of hydropower stations along rivers. In addition to generating electricity, some hydropower stations can regulate their own reservoir capacity and control the water flow of upstream and downstream rivers. They also bear part of the flood control pressure while increasing the power generation to ensure flood control safety. Today, in the context of striving to reach the peak of carbon dioxide emissions by 2030 and to achieve carbon neutrality by 2060, China's energy structure will accelerate its transformation to a low-carbon and clean direction. The proportion of renewable energy power generation represented by hydropower will further increase.

With more generating capacity undertaken by hydropower stations, the number and scale of giant Francis turbine units are increasing gradually. The size and weight of the components of giant units are often large, and the internal structure and processing technology are complex. In particular, the runner blades are vulnerable to the dynamic loads generated by pressure pulsation and various mechanical disturbances, which lead to the vibration and cracking of the blades. Therefore, the assembly accuracy and quality of the unit are crucial for the safe and reliable operation of the unit after it is put into production. The Francis turbine includes a spiral case, stay vane, guide vane, runner, head cover, pressure balance pipe, draft tube, stay ring, and other structures. Given the large size of the giant Francis turbine, the leakage and volume loss of upper crown clearance, lower band clearance, and labyrinth ring caused by the gap between the runner and fixed parts are also large [1,2]. The pressure pulsation caused by these fluids is one of the main reasons affecting stable operation. The pressure pulsation of the Francis turbine refers to the alternating random change of water pressure around its average value in the flow passage, which contributes to the vibration of the hydraulic turbine generator unit [3]. So far, most scholars have mainly studied the vaneless area, runner, draft tube, and leakage water through the combination of numerical simulation [4,5] and test [6]. Through their characteristic frequency and amplitude, they can have a deeper understanding of the flow characteristics and vibration mechanism of the internal flow field [7–9]. Trivedi [10] studied the vaneless area of the turbine and pointed out that the frequency of pressure fluctuation in the rotating and stationary passage is mainly related to the number of guide vanes and runner blades and the frequency of rotation. The two passages are mainly affected by the runner and the guide vanes respectively. Under low load conditions, vortex ropes will appear in the draft tube. Arpe [11] and others found that the frequency of the vortex rope in the draft tube is mainly 0.2–0.4 times the rotational frequency by studying the pressure pulsation of the straight and elbow section of the draft tube. There will also be the frequency of the vortex rope in the vaneless area, indicating that the vortex rope also has an impact on the flow characteristics in the vaneless area. A large number of studies [12,13] show that pressure pulsation will generate noise and vibration, which seriously threatens the stable operation of the unit. Through CFD simulation, Liang Wuke [14] compared the full-flow passage simulation with and without cavities and found that the cavity has a great influence on the runner stress. So cavities should not be ignored in the study of hydraulic axial force. As a structure to reduce leakage and increase efficiency, Sun Huifang [15] and others found that the farther the labyrinth ring is away from the central axis, the greater the influence on the axial water force. However, although the accuracy of the labyrinth ring is improved, the calculation cost is increased. The pressure balance pipe connects the clearance with the draft tube to balance the water pressure in the clearance, so as to reduce the impact on the hydraulic axial force and the load on the force bearing. Qu Boxing [16] analyzed the structure of the pressure balance pipe and the cause of water leakage through examples and proposed improvement measures.

The giant Francis turbine is easy to cause large hydraulic axial force, and its safe, efficient, and stable operation affects the entire power supply system significantly. As a result, the design and selection of runners and other structures are very important. The hydraulic axial force of the turbine refers to the axial component force of water flow acting on the runner, mainly including the axial force on the surface of the runner hub, shroud,

blade, upper crown clearance, and lower ring clearance [17]. The calculation methods of hydraulic axial force are mainly theoretical formula [18], numerical simulation [19], and experimental measurement [20]. Nevertheless, the traditional methods generally rely on experience and assumptions [21,22], and only consider the constant value, which cannot show the pressure pulsation and the pulsation of axial hydraulic force. Consequently, sometimes there is a large deviation. After the continuous improvement of the calculation method, the accuracy of the hydraulic axial force calculation results has been significantly improved [23]. Compared with the prototype test measurement, Li Haoliang [19] and Ji Xingying [24] proposed a more efficient and accurate axial force calculation method based on numerical simulation calculation.

The hydraulic axial force of the hydraulic turbine has a great influence on the structural design and stable operation of the unit. Too much downward will cause overload and damage to the force bearing [25]. Too much upward will lead to serious turbine lifting and severe vibration [26], which will seriously affect the operation of the hydropower station. A large number of studies have shown that the hydraulic axial force is related to the pressure distribution [27–30]. Xiao Ruofu [31] and others analyzed the dynamic stress of the Francis turbine based on fluid–structure coupling and found that the dynamic stress resulting from the hydraulic force is one of the main factors causing the fatigue crack of the runner blade. Li Xiangyang [32] considered that the pressure difference between the upper crown clearance and the runner’s internal passage is the main factor leading to the axial force, which is mainly induced by the flow pattern in the runner. For pumped storage units with frequent startup and shutdown, when the input force of the pump mode gradually decreases, the hydraulic axial force will suddenly change and have an impact on the stable operation of the unit [33,34]. When the pump and turbine modes are switched, the hydraulic axial force will have a peak value [35]. To reduce the harm of the axial force, sealing device, pressure-reducing plate, and drain hole [36], the pressure balance pipe and other equipment [37] are generally set in the actual project.

The sealing device is designed to reduce leakage since the hydraulic axial force increases with the raise of flow and head [38]. The pressure-reducing plate is fixed on the top cover of the turbine by using rib plates and reduces the volume of rotating water flow in the clearance [39] to reduce the axial force of the turbine. The pressure balance pipe uses the pressure difference between the clearance and the draft tube to discharge the leakage water in the clearance to the draft tube. Compared with other methods, the pressure balance pipe reduces the pressure in the clearance and is used more and more widely in practical projects.

To date, most of the literature studies lack research on the hydraulic axial force of Francis turbines containing clearance and pressure balance pipes [40], especially for the prototype units of giant hydraulic turbines with the larger size, higher requirements on operation stability and installation accuracy. Hence, the flow pattern in the runner and clearance passage and the trend of the hydraulic axial force of each surface of the runner with the different axial installation deviations of the runner under the rated working conditions are calculated. The influence of uncertain factors such as the shape of the runner passage on the hydraulic force is studied, so as to better understand the characteristics of the internal force of the turbine and provide guidance for the design, manufacturing, and installation.

In this study, the influences of the axial installation deviation of the runner on the hydraulic axial force of the 1000 MW Francis turbine unit are investigated.

## 2. Methodology

### 2.1. Three-Dimensional Control Calculation Equation

The flow in giant Francis turbine units has high Reynolds numbers, and the flow is nonlinear, multiscale unsteady, and complex turbulence. It is generally difficult to directly solve the NS (direct numerical simulation) equation with a computer. Some experts have used OpenFOAM with different turbulence models, including a large eddy model to

investigate the fluid flow [41–44]. Therefore, the turbulence model in the current research generally is simplified appropriately, and some unimportant details are ignored. In this paper, the Reynolds average method, one of the indirect numerical simulation methods, is used to decompose the turbulent velocity and pressure into the sum of the average and the pulsation. The conversion of mechanical energy is only concerned about in this paper, so the internal flow control equations of giant turbines only have mass conservation equations and momentum conservation equations. For the internal flow of fluid machinery, it can be considered that the fluid is incompressible, and its flow law is described by the following basic hydrodynamic equations [45]:

$$\frac{\partial}{\partial x_i}(\bar{u}_i) = 0 \quad (1)$$

$$\frac{\partial}{\partial t}(\bar{u}_i) + \frac{\partial}{\partial x_j}(\bar{u}_i \bar{u}_j) = -\frac{1}{\rho} \frac{\partial \bar{p}}{\partial x_i} + \frac{\partial}{\partial x_j} \left[ v \left( \frac{\partial u_i}{\partial x_j} + \frac{\partial u_j}{\partial x_i} \right) \right] - \frac{\partial \overline{u'_i u'_j}}{\partial x_i} + f_i \quad (2)$$

where  $x_i, x_j$  represent coordinates,  $u_i, u_j$  represent the three directional components of velocity in the rectangular coordinate system and the indicators  $i$  and  $j$  are the three-dimensional coordinate directions.  $\rho$  is density.  $v$  is kinematic viscosity.  $t$  is time.  $p$  is pressure, and  $f_i$  is volume force. The RANS equation is similar to the original NS equation, except that a new unknown Reynolds stress  $\overline{u'_i u'_j}$  is introduced. Thus, the Reynolds stress is connected with the turbulence mean to close the equations.

## 2.2. Turbulence Model

Turbulence models are generally two-equation turbulence models to solve the velocity scale and length scale. With the continuous development of computational fluid dynamics, various turbulence models with different characteristics have emerged. Turbulent kinetic energy  $k$  is the average kinetic energy of unit mass pulsating motion. The Boussinesq assumption is adopted in the eddy viscosity model, and the Reynolds stress is compared with the viscous stress. It is considered that the Reynolds stress is related to the average velocity gradient and eddy viscosity coefficient, and the relationship is as follows.

$$-\overline{u_i u_j} = v_t \left( \frac{\partial \bar{u}_j}{\partial x_i} + \frac{\partial \bar{u}_i}{\partial x_j} \right) - \frac{2}{3} k \delta_{ij} \quad (3)$$

The general eddy viscosity coefficient  $v_t$  mainly adopts the  $k - \omega$  model and corresponding improved models. These models are based on the relevant equations of turbulent kinetic energy  $k$ , turbulent dissipation rate  $\mathcal{E}$ , or turbulent frequency  $\omega$  to close the equations. The equations of turbulent kinetic energy  $k$  and dissipation rate  $\mathcal{E}$  are as follows:

$$k = \frac{1}{2} \overline{u_i u'_i} \quad (4)$$

$$\varepsilon = v \left( \frac{\partial u'_i}{\partial x_j} \right) \left( \frac{\partial u'_i}{\partial x_j} \right) \quad (5)$$

The  $k - \mathcal{E}$  turbulence model has a high accuracy to simulate three-dimensional fluid turbulent flow, which belongs to the high Reynolds number turbulence model. However, there is a deviation in the calculation of the anisotropy that needs to consider the turbulent viscosity, and it is difficult to accurately predict the flow with reflux and strong swirl. RNG  $k - \mathcal{E}$  modified the transport equation of dissipation rate  $\mathcal{E}$ , considering the factors of rotation rate and strain rate, and improved the simulation of rotating turbulence and large curvature flow. The  $k - \mathcal{E}$  model is insensitive to the adverse pressure gradient and always simulates excessive shear stress. The  $k - \omega$  model closes the time-averaged N-S equation by introducing turbulent kinetic energy  $k$  and turbulent frequency  $\omega$ . The accuracy of

boundary layer calculation is improved, and the necessary nonlinear damping function in the  $k - \mathcal{E}$  model is not included. There is little difference between the calculated and actual results of  $k - \mathcal{E}$  model in the wake, mixed flow, and flow around a cylinder. However, in the free shear flow, the turbulent dissipation rate  $\omega$  has too much influence on the  $k - \mathcal{E}$  model results. The eddy viscosity coefficient in the standard  $k - \mathcal{E}$  model is defined as:

$$v_t = \frac{k}{\omega} \quad (6)$$

SST  $k - \omega$  (shear stress transport  $k - \omega$  Model) combines the advantages of  $k - \mathcal{E}$  model and  $k - \omega$  model. It uses the  $k - \omega$  model in the near wall area and the  $k - \mathcal{E}$  model in the turbulent core area. Because of its coupling and considering the transmission of turbulent shear stress, the SST model can predict flow separation well. This model has great advantages in predicting near-wall flow and adverse pressure gradient flow.

$$\frac{\partial(\rho_m k)}{\partial t} + \frac{\partial(\rho_m u_i k)}{\partial t} = P_k - \frac{\rho_m k^{3/2}}{l_{k-\alpha}} + \frac{\partial}{\partial x_i} \left[ \left( \mu + \frac{\mu_c}{\sigma_k} \right) \frac{\partial k}{\partial x_i} \right] \quad (7)$$

$$\frac{\partial(\rho \omega)}{\partial t} + \frac{\partial(\rho u_i \omega)}{\partial x_i} = C_\omega P - \beta \rho \omega^2 + \frac{\partial}{\partial x_i} \left[ (\mu_l + \sigma_\omega \mu_t) \frac{\partial \omega}{\partial x_i} \right] + 2(1 - F_1) \frac{\rho \sigma_\omega}{\omega} \frac{\partial k}{\partial x_i} \frac{\partial \omega}{\partial x_i} \quad (8)$$

where  $\rho_m$  is the fluid density,  $P$  is the turbulence generation term,  $F_1$  is the mixing function,  $k$  is turbulent kinetic energy,  $\omega$  is turbulent frequency,  $\mu$  is dynamic viscosity. The empirical coefficients are  $\sigma_k = 2$ ,  $\beta = 0.0828$ ,  $\sigma_\omega = 0.856$ .

### 3. Numerical Calculation and Design of Flow Field

#### 3.1. Fluid Passage Model and Main Parameters

The parameters of the giant Francis turbine studied in this paper are shown in Table 1. The calculation passage is from the spiral case inlet to the draft tube outlet, mainly including the spiral case, stay vane, guide vane, runner, upper crown clearance, lower band clearance, draft tube, discharge cone, and pressure balance pipe. The pressure balance pipe connects the upper crown clearance and the draft tube. The final three-dimensional model is shown in Figure 1. To obtain more accurate information such as the hydraulic force of the turbine, the runner's upper crown and lower band leakages and pressure balance pipe are also simulated and analyzed. The hydraulic force of the runner and clearance flow acts on the fluid–structure interface, including the blade surface (BS), the upper crown outer surface (UCOS), the upper crown inner surface (UCIS), the lower band outer surface (LBOS), the lower band inner surface (LBIS), and the discharge cone surface (DCS). These surfaces are illustrated in Figure 2.

**Table 1.** The Parameters of giant Francis turbine.

| Parameter               | Value      |
|-------------------------|------------|
| Specific speed          | 146.7 m·kW |
| Unit volume flow        | 755.6 L/s  |
| Number of guide vanes   | 24         |
| Number of runner blades | 15         |
| Number of stay vanes    | 23         |

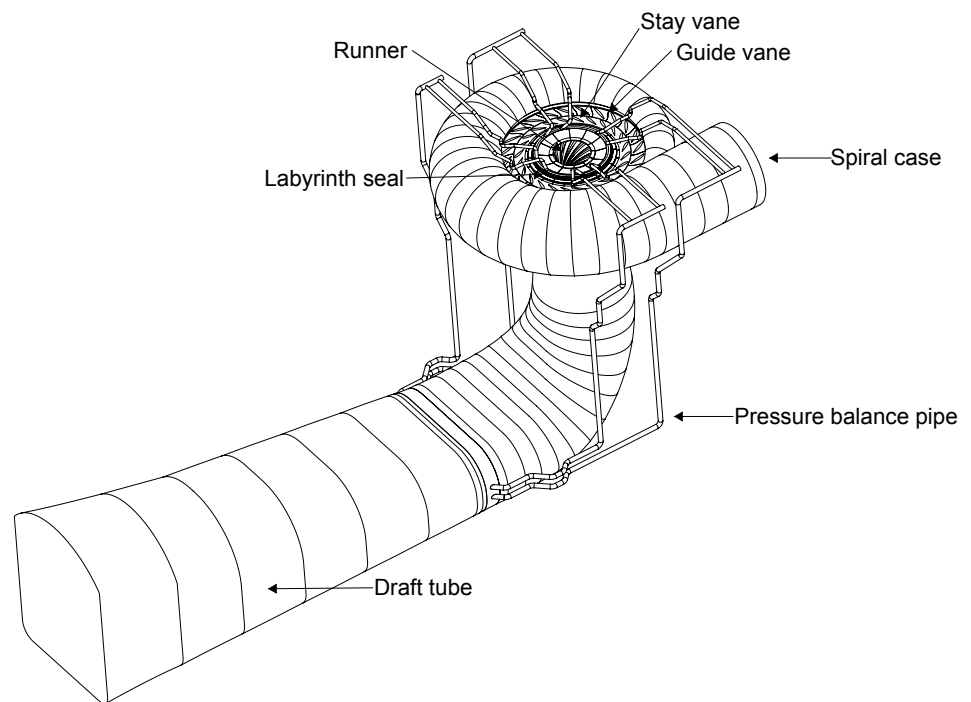


**Figure 1.** Overview of the 3D flow profile of the turbine.

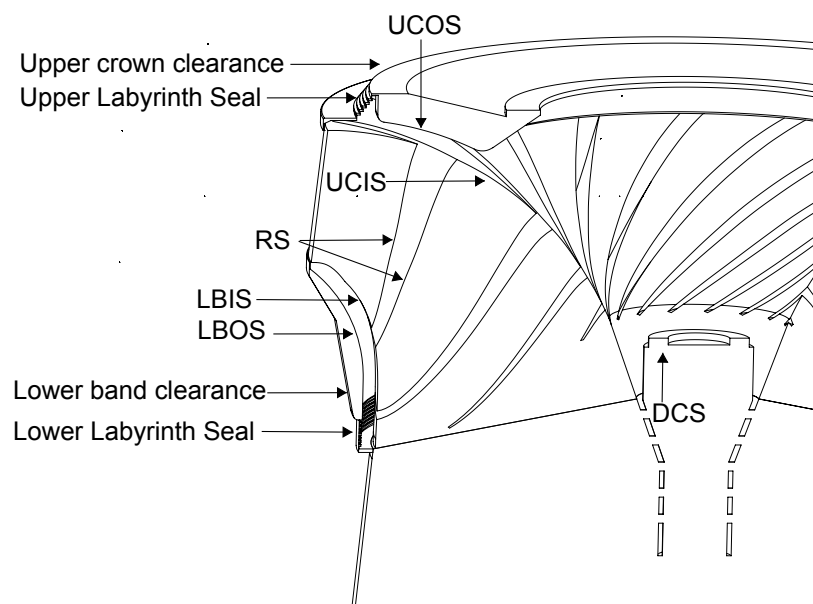


**Figure 2.** Details of clearance passage.

### 3.2. Mesh of Flow Field and Calculation Condition Setting

Considering the focus of this paper and the structural characteristics of the model, the structured hexahedral mesh and unstructured tetrahedral mesh are finally selected to discretize the flow field of the giant Francis turbine. The number and size of mesh elements at key locations are controlled to improve the calculation accuracy and efficiency. Since the passage structure of the spiral case and discharge cone is complex and contains a large number of irregular surfaces, tetrahedral mesh with better flexibility and adaptability is used for division. The structures of the stay vane, guide vane, runner, draft tube, upper and lower clearance flow passage, and pressure balance pipe are more regular, and the hexahedral structure mesh with more saving storage space and a faster calculation speed is used for division. The mesh of the runner and its seal and clearance is densified to ensure a

more accurate calculation of the hydraulic axial force of the runner and its upper and lower seals. Because the main flow area near the entrance of the upper and lower clearance is a vaneless passage with a large mesh size, the boundary layer of the vaneless passage is locally densified to reduce the error caused by the mesh size difference between the two flow passages. Similarly, the outlet of the lower band gap is mainly connected with the inlet section of the draft tube, thus the mesh at the junction is also partially densified. The overall mesh quality is great, and the mesh generation results are shown in the following Figure 3.

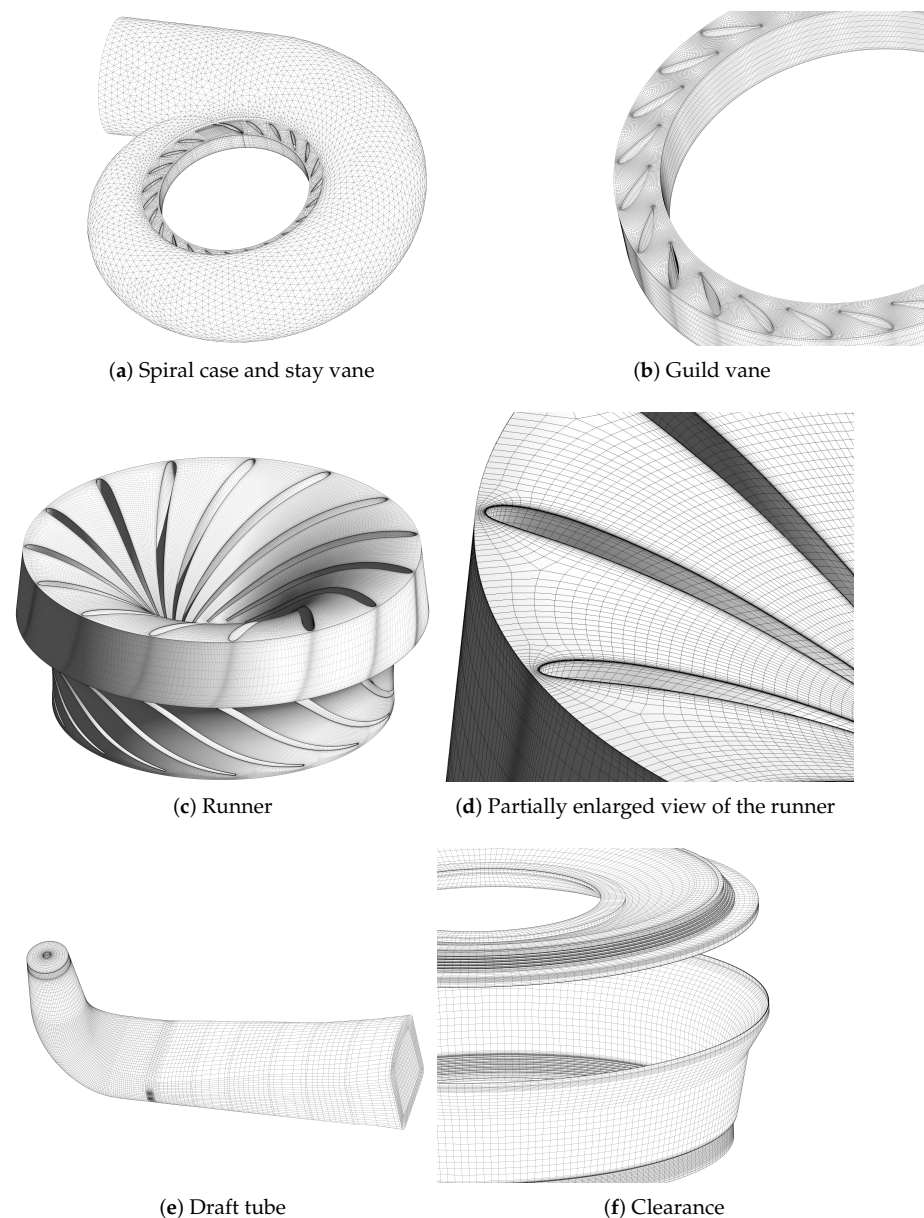


**Figure 3.** Mesh of the flow passage.

According to previous practical experience and simulation research, the internal flow field of the giant Francis turbine is complex. Therefore, the calculation of runner installation with different axial sinking values under the rated head is carried out. The parameters of the studied operating condition are shown in Table 2, and a total of seven deviation models of 0, 0.5, 1, 1.5, 2.5, 4, and 5.5 mm are taken. To prevent the calculation influence brought by the mesh, the mesh discretized law and quantity of the clearance passage, runner passage and draft tube passage of different deviation models are consistent. Through the

numerical simulation of the steady flow in the full flow channel of the Francis turbine, the flow characteristics of the Francis turbine under different installation deviations are studied. The calculation passage is incompressible fluid from the turbine spiral case inlet to the draft tube outlet. ANSYS CFX, a widely used CFD code for academic research and industrial applications, is selected to calculate the fluid dynamic characteristics of the 1000 MW Francis turbine in this investigation. The calculation model is SST  $k - \omega$ . The inlet condition is set as the total pressure boundary. The static pressure boundary is set at the outlet. The pressure value is determined according to the downstream tail water level of the power station and the installation elevation of the power station. The inlet pressure and the guide vane opening are determined according to the actual working conditions. The UCOS and LBOS are set to rotate at the same speed as the runner. All other walls are non-slip walls. The runner passage is set to rotate at 111.1 r/min. Other passages are static. The dynamic interfaces between the runner and upstream and downstream components are set as Frozen Rotor, and the other interfaces are set as General Connection. The convergence residual is set to  $10^{-5}$  in the steady calculation. The time step is set to 0.0045 s and the number of iterations is 20,000.

**Table 2.** Parameters under the rated operating condition.

| Guide Vane Opening (°) | Head (m) | Output (MW) | Flow Rate (m <sup>3</sup> /s) |
|------------------------|----------|-------------|-------------------------------|
| 27.8                   | 202      | 1015        | 545.49                        |

### 3.3. Mesh Independence Analysis

To reduce the influence of the number of mesh on the calculation results, the Richardson extrapolation method is used to verify the mesh independence [46,47]. The basic idea is to establish a relationship based on the proportion between the approximation error and the real error. A total of four groups of different mesh elements ( $3.04 \times 10^6$ ,  $5.0 \times 10^6$ ,  $1.02 \times 10^7$ ,  $2.0 \times 10^7$ ) are set up, and the efficiency of the giant turbine under steady-state rated conditions is analyzed with the change of mesh elements (refer to Table 3). The third set of meshes with around 10.5 million elements marked with circle in the Figure 4 was adopted for further simulation. The mesh detail of each passage is listed in Table 4.

**Table 3.** Measurement and simulation results.

|                    | Head H (m) | Output (MW) | Flow Rate (m <sup>3</sup> /s) |
|--------------------|------------|-------------|-------------------------------|
| Model test         | 202        | 1015        | 545                           |
| $3.04 \times 10^6$ | 202        | 1026        | 560                           |
| $5.0 \times 10^6$  | 202        | 1037        | 578                           |
| $1.02 \times 10^7$ | 202        | 1070        | 586                           |
| $2.0 \times 10^7$  | 202        | 1071        | 587                           |

**Table 4.** Number of elements in each passage.

| Component             | Elements (Million) | Element Type               |
|-----------------------|--------------------|----------------------------|
| Spiral case           | 1.55               | tetrahedral                |
| Stay vane             | 0.38               | hexahedral                 |
| Guide vane            | 0.76               | hexahedral                 |
| Runner                | 2.47               | hexahedral                 |
| Upper crown clearance | 0.78               | tetrahedral and hexahedral |
| Lower band clearance  | 2.47               | hexahedral                 |
| Draft tube            | 0.93               | tetrahedral and hexahedral |
| Pressure balance pipe | 1.04               | hexahedral                 |
| Discharge cone        | 0.13               | tetrahedral                |
| Total                 | 10.5               | tetrahedral and hexahedral |

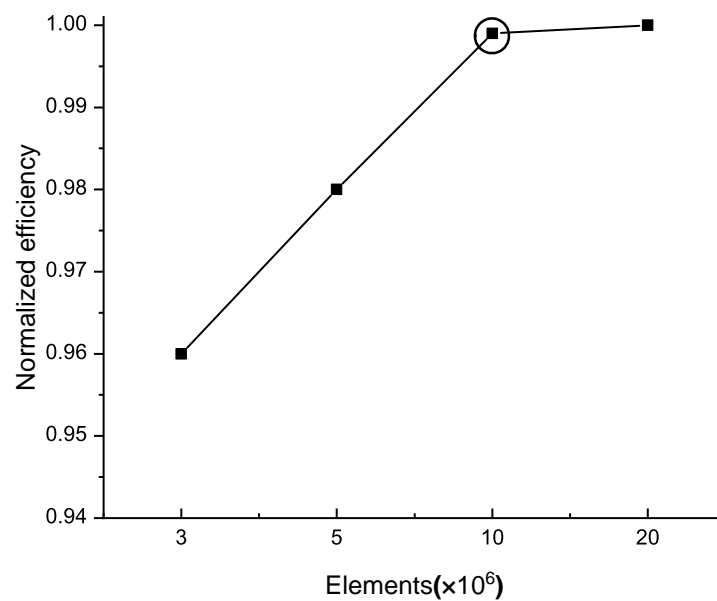


**Figure 4.** Mesh independence analysis.

The accuracy of the model turbine in the manufacturing process, the flow of internal clearance, and the difference in boundary conditions will cause some inevitable errors between the test value and the calculated value. In this case, it is necessary to verify the model before numerical calculation, and relying on the actual model for numerical calculation has practical engineering significance. To verify that the error between the calculated results and the measurement results is within a reasonable range, the efficiency values under different heads of the same guide vane opening are calculated and compared with the test results. The results are shown in Figure 5. From the comparison results, the error between the calculation efficiency and the test results does not exceed 5%. The changing trend is the same with the increase of guide vane opening, which meets the reliability requirements of numerical simulation. In summary, the numerical simulation method used in this paper is reliable, and the results have high reference values for engineering applications.

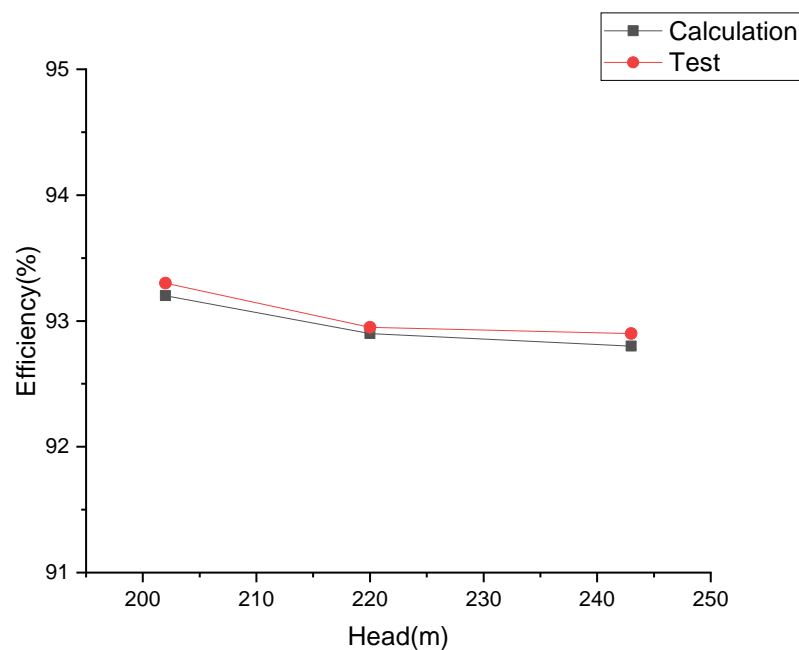


**Figure 5.** Efficiency comparison between simulation and measurement.

### 4. Results and Discussions

#### 4.1. Characteristic of Hydraulic Axial Force

The formula for calculating the total hydraulic axial force  $F$  of the mixed flow pump turbine is shown in Equation (9), which specifies that the axial force is positive upward. The specific composition of the hydraulic axial force of the Francis turbine is shown in Figure 6.  $F_1$  is the downward force on the UCOS of the runner from the upper crown clearance inlet to the main shaft seal.  $F_2$  is the upward force on the LBOS of the runner from the inlet to the outlet of the lower band clearance.  $F_3$  is the upward force acting on the UCIS of the runner.  $F_4$  is the downward force acting on BS.  $F_5$  is the downward force acting on the LBIS of the runner.  $F_6$  is the upward force acting on DCS. In this paper, the hydraulic axial forces of different surfaces with the runner installation droppings of 0 mm, 0.5, 1, 1.5, 2.5, 4, and 5 mm are calculated. The calculation results are shown in the following Table 5.

$$F = F_1 + F_2 + F_3 + F_4 + F_5 + F_6 \tag{9}$$

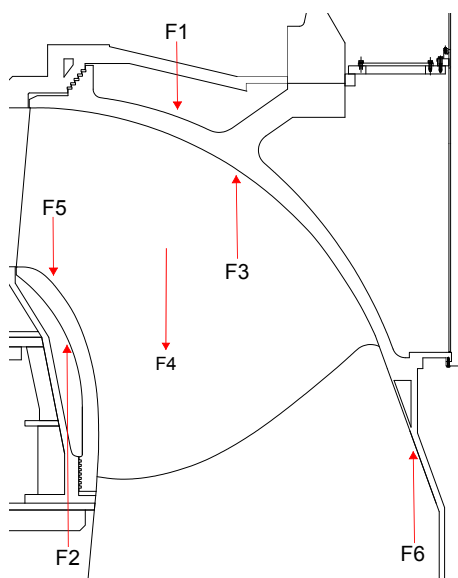


Figure 6. Hydraulic axial force distribution.

Table 5. Calculation results of the hydraulic axial force.

| Runner Dropping Distance (mm) | $F (\times 10^4 \text{ N})$ | $F_1 (\times 10^4 \text{ N})$ | $F_2 (\times 10^4 \text{ N})$ | $F_3 (\times 10^4 \text{ N})$ | $F_4 (\times 10^4 \text{ N})$ | $F_5 (\times 10^4 \text{ N})$ | $F_6 (\times 10^4 \text{ N})$ |
|-------------------------------|-----------------------------|-------------------------------|-------------------------------|-------------------------------|-------------------------------|-------------------------------|-------------------------------|
| 0                             | 1030                        | −3050                         | 2222                          | 4540                          | −949                          | −1803                         | 69                            |
| 0.5                           | 1010                        | −3052                         | 2204                          | 4538                          | −949                          | −1800                         | 69                            |
| 1                             | 995                         | −3054                         | 2194                          | 4536                          | −947                          | −1803                         | 69                            |
| 1.5                           | 975                         | −3060                         | 2183                          | 4538                          | −949                          | −1805                         | 69                            |
| 2.5                           | 955                         | −3072                         | 2168                          | 4543                          | −949                          | −1804                         | 69                            |
| 4                             | 931                         | −3074                         | 2154                          | 4538                          | −949                          | −1807                         | 69                            |
| 5.5                           | 928                         | −3080                         | 2153                          | 4541                          | −948                          | −1807                         | 69                            |

It is generally believed that the diameter of the labyrinth ring is basically equal, which can make the hydraulic axial forces (acting on the upper and lower surfaces of the runner) equal. However, the calculation result is not the same. Compared with  $F_2$  and  $F_5$ , the hydraulic axial forces of  $F_1$  and  $F_3$  are larger. This is because the horizontal area of the upper crown is relatively large, and they are vulnerable to the impact of axial force. The UCIS changes the flow direction of water, so the UCIS has the largest axial force. The horizontal area of RS is small, and the pressure on the pressure surface is greater than the pressure on the suction surface. So under the superposition of the two,  $F_4$  is small and

downward. With the decline of runner installation, F3, F4, F5, and F6 in the runner flow channel do not change much. This is because the dropping of the runner installation does not affect the flow rate and flow pattern in the runner channel, so the impact can be ignored. Nevertheless, other axial forces fluctuate greatly. All points of hydraulic axial force  $F$  are fitted with a curve of a quadratic polynomial, and the result is  $y = -41x + 4.07x^2$ . The curve of  $F$  with the deviation distance of the axial installation of the runner is shown in Figure 7. It can be seen that  $F$  drops rapidly at the beginning as the runner drops. However,  $F$  changes little with the decline of the runner when the runner descends to 4mm, indicating that the downward installation at this time has little impact on the overall hydraulic axial force of the runner. Similar to the trend of  $F$ , the distribution of  $F1$  on UCOS and  $F2$  on LBOS also tends to be stable as the runner is installed downward. Using the same method, the points of  $F1$  and  $F2$  changing with the axial installation distance are fitted by the quadratic polynomial, and the curve of  $F1$  is  $y = 10.09x - 0.77x^2$ , which is shown in Figure 8. The curve of  $F2$  is  $y = -27.42x + 2.759x^2$ , as shown in Figure 9.

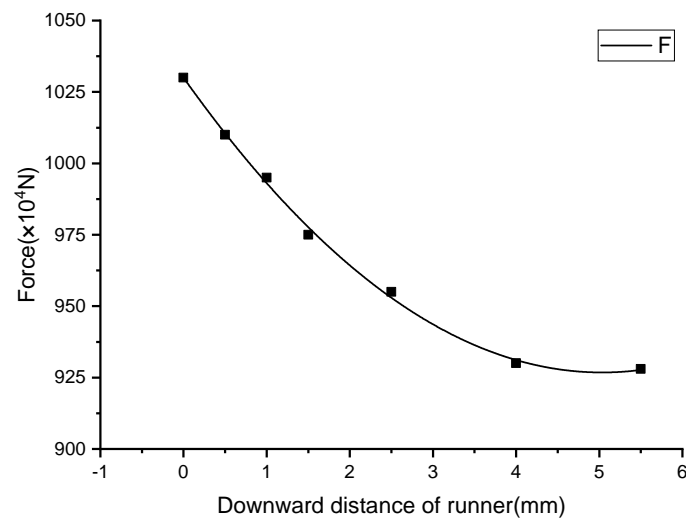


Figure 7.  $F$  variation with the dropping distance of the runner.

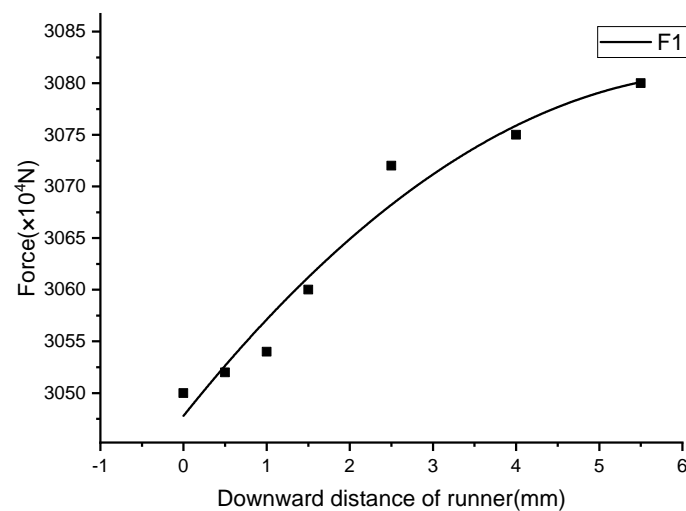
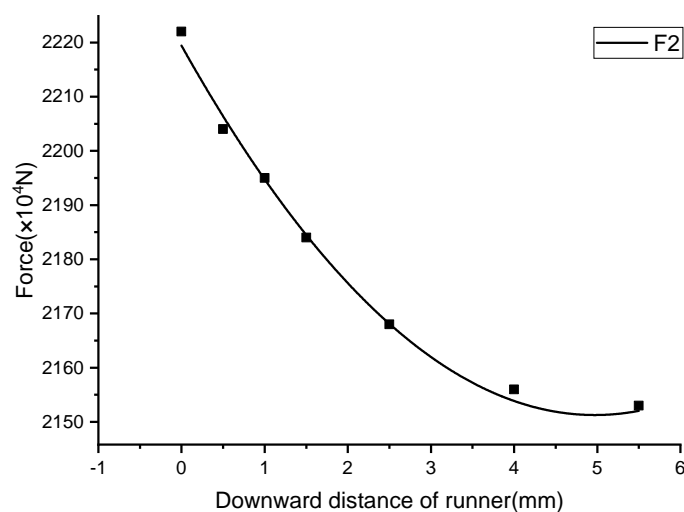


Figure 8.  $F1$  variation with the dropping distance of the runner.



**Figure 9.** F2 variation with the dropping distance of the runner.

The reason for this phenomenon may be related to the clearance leakage and the internal flow pattern of the clearance. Therefore, the leakage and internal flow patterns of different runner dropping are compared. Table 6 is the leakage rate of the upper crown and the lower band clearance of the runner. It can be seen that as the runner decreases, the leakage rate of the upper crown clearance and the lower band clearance does not increase or decrease monotonously. When the runner drops to 0.5 mm, the leakage of the lower ring increases first, then decreases and gradually approaches a stable value as the runner continues to decline. It is not exactly the same as the change rule of F2. Although the volume of the upper crown clearance will increase while the runner drops. The leakage of the upper crown clearance will basically remain between 910 and 920 kg/s, and maintain at 910 after the runner drops to 2.5 mm. It shows that the leakage will have a certain impact on the axial force of the runner, but it is not necessarily the same as the changing trend of the axial force.

**Table 6.** Leakage rate variation with the dropping distance of the runner.

| Runner Dropping Distance (mm) | Lower Band Leakage Rate (kg/s) | Upper Crown Leakage Rate (kg/s) |
|-------------------------------|--------------------------------|---------------------------------|
| 0                             | 1771                           | 919                             |
| 0.5                           | 1814                           | 916                             |
| 1                             | 1799                           | 912                             |
| 1.5                           | 1797                           | 920                             |
| 2.5                           | 1776                           | 910                             |
| 4                             | 1769                           | 910                             |
| 5.5                           | 1765                           | 910                             |

#### 4.2. Mechanism Discussion

##### 4.2.1. Pressure Distribution on Section ZX

To analyze the change of hydraulic force induced by runner axial installation deviation, the pressure distribution of the ZX section under different deviation models was studied. It was found that the static pressure distribution on the ZX section of the deviation model was similar to that without deviation. It means the drop of the runner has little effect on the pressure distribution of the runner and upper crown and lower band. Therefore, the pressure distribution of the ZX section in the runner and clearance flow passage with 0 mm runner drop and 5.5 mm runner drop are listed as shown in Figure 10. The pressure in the clearance and the runner gradually decreases along the flow channel and the fastest decline is in the labyrinth ring of the clearance. After the flow comes out of the labyrinth ring, the sectional area of the clearance passage gradually increases. A large low-pressure area is

generated at the upper crown and the outlet of the lower band, which results in unstable flow. When the pressure in the clearance is lower than the saturated vapor pressure of the water flow at the corresponding temperature, a vortex rope will be generated. As the runner decreases, the pressure decreases gradually near the entrance of the lower band, while in the upper crown section, the pressure only fluctuates near the main shaft. The pressure distribution and values in the runner passage of different deviation models are not much different, so the axial force on RS, UCIS, and LBIS remains stable. It can be considered that the axial force on UCIS and LBIS is little affected by the installation deviation of the runner. At the same XY coordinate, along the Z-axis, the pressure of the upper crown clearance is significantly less than that of the runner passage, so F1 is clearly larger than F3. Similarly, the pressure difference between LBIS and LBOS is not significant, and the difference between F2 and F5 is not much. Therefore, the dropping of the runner mainly leads to the change of the flow pattern in the upper crown and the lower band clearance, which affects the change of the axial force. The relative pressure coefficient  $C_p$  is defined as:

$$C_p = \frac{P}{\rho g H_r} \quad (10)$$

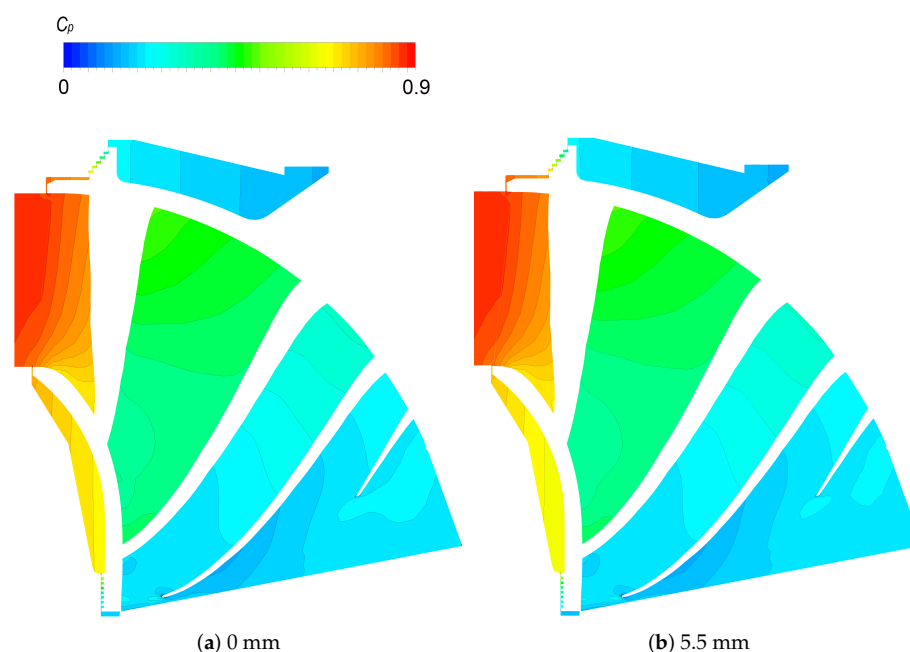


**Figure 10.** Pressure distribution of the ZX section in the runner and clearance passage.

#### 4.2.2. Hydraulic Force on the Surface of Clearance

The hydraulic force distribution on UCOS of the upper crown clearance is shown in Figure 11. The difference of runner dropping models is mainly at the horizontal position of the upper crown in front of the labyrinth ring entrance and inside the cavity. When the runner moves 1 mm downward from 0 deviation, the hydraulic force at the horizontal crown decreases, while the hydraulic force at some positions in the cavity increases. The installation position of the runner continues to move downward from 1 mm, and the overall axial force distribution is basically not much different, but the axial force at the horizontal position of the upper crown (HPUC) becomes larger and reaches a peak. The further downward movement of the runner will not affect the distribution of the hydraulic force, while the force at the cavity position changes greatly. Moreover, the distribution law is obviously different from the results of other deviation models. The runner continues to move down to between 4 and 5.5 mm, and the axial force distribution at the cavity and HPUC remains basically unchanged, with only a small range of numerical fluctuations.

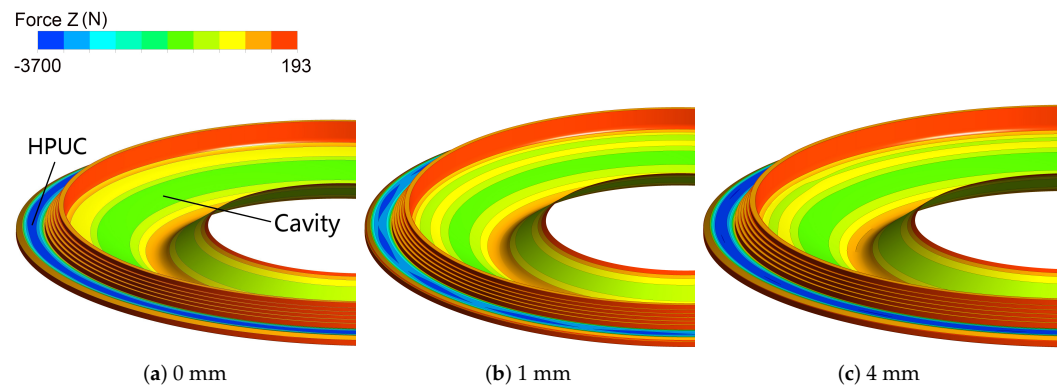


**Figure 11.** Hydraulic force distribution on UCOS.

The hydraulic force distribution on the LBOS of the lower band is shown in Figure 12. From top to bottom, the hydraulic force on the LBOS increases first and then decreases, and reaches the maximum at the sudden expansion place near the inlet. The distribution laws of different deviation models are similar with only slight differences. When the runner drops from 0 to 5.5 mm, there will be a slight periodic fluctuation along the axial direction at the sudden expansion place of the lower band inlet. However, the change is very small, and the axial force in the middle of the vertical direction also changes.

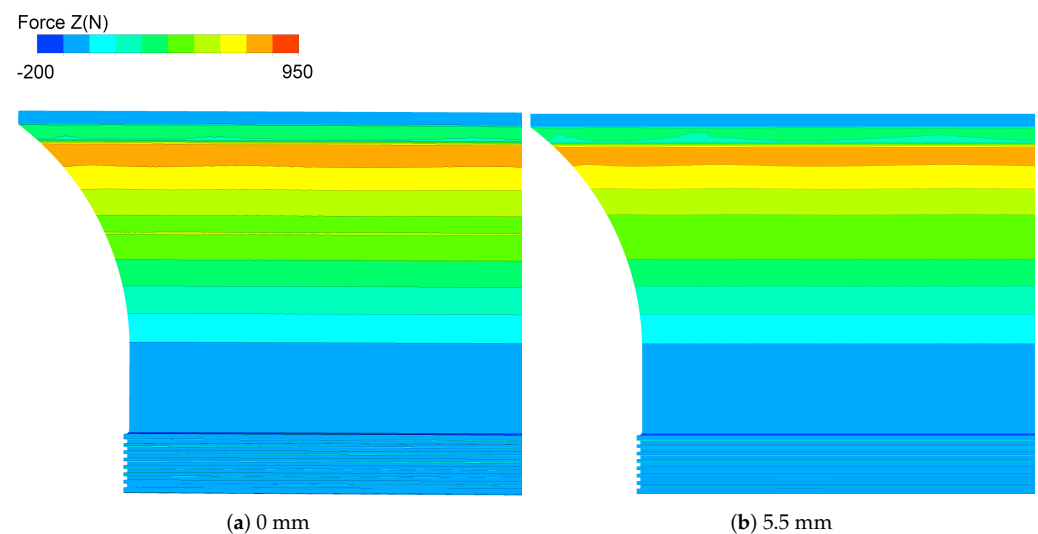


**Figure 12.** Hydraulic force distribution on LBOS.

#### 4.3. Streamlines in Clearances

Figure 13 shows the X1–X15 sections in the lower band clearance and the S1–S15 sections in the upper crown clearance. The X1–X15 sections are between the two runner blades from the circumferential direction, and the S1–S15 sections are between the inlet of the two pressure balance pipes. Figure 14 is the streamline and relative velocity coefficient  $C_v$  distribution of the X1–X15 sections with the 0 mm movement of the runner under rated conditions. The internal flow pattern of the lower band clearance is more disordered, and the size of the clearance changes greatly along the flow passage. The separation flow caused by the expansion of the area and the inclination angle lead to the emergence of the corner vortex, and the flow direction of the vortex on the rotating wall side was opposite to that on the stationary wall side. Observing the streamlined distribution from X15 to X1, the vortex near the fixed wall at the sudden-expansion of the lower band inlet gradually moves downward and disappears at X5. At the same time, a new vortex 1 is generated and becomes a large vortex at X1. When the vortex moves below the right vortex 2, the

right vortex is divided into vortex 2 and vortex 3. The newly generated vortex 3 moves downward and is eventually swallowed by the following large vortex 4. The vortex 4 always exists in the lower band clearance. The whole process has obvious periodicity in the middle of every two blades. With the decrease in the installation position of the runner, the streamlined distributions of the X1–X15 sections are similar, only slightly different in the flow rate.  $D$  is the diameter of the runner. The relative velocity coefficient  $C_v$  is defined as:

$$C_v = \frac{v}{\frac{\pi n D}{60}} \quad (11)$$

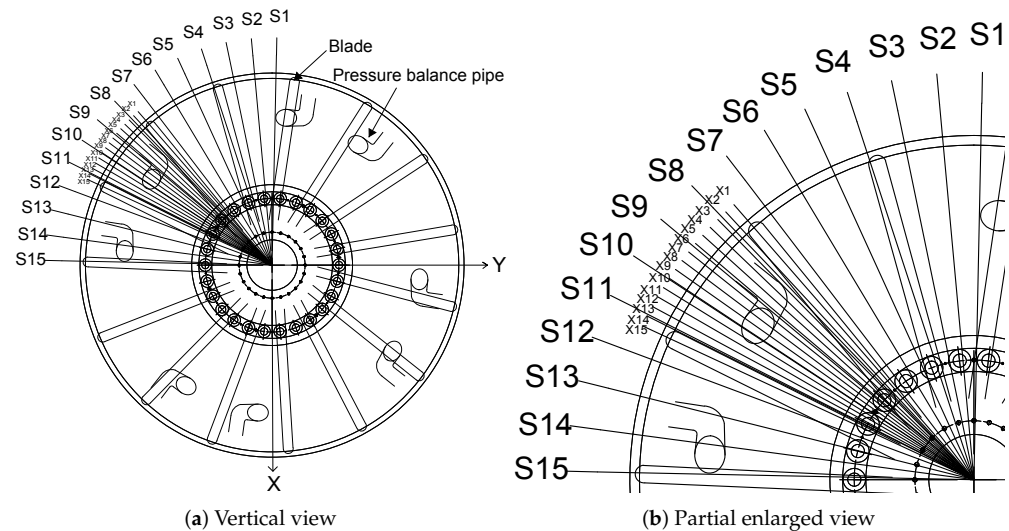


**Figure 13.** Flow monitoring section distribution of clearance.

Figure 15 is the streamlined and relative velocity coefficient  $C_v$  distribution of the S1–S15 section of the upper crown clearance with 0 deviation of the runner. High-speed water flows from the inlet of the upper crown clearance into the labyrinth ring along the wall of the upper crown. There are obvious vortices in the labyrinth ring. The water enters the cavity after coming out of the labyrinth ring. The flow pattern in the cavity is disordered and there are vortices regions. The vortex adhering to the stationary wall rotates in the opposite direction to that on the rotating wall. From S15 to S12, there is a vortex near the UCOS of the cavity. The vortex gradually moves upward to the head cover, and then gradually expands. The vortex almost fills the cavity near S6 and then moves downward. These vortex structures will cause uneven stress on local surfaces. On the other hand, the hydraulic axial force on the outer surfaces of the upper crown and lower band will have pulsating characteristics of corresponding frequencies. As the installation position of the runner decreases, the streamlined distribution of the upper crown section remains unchanged, but the position and speed of the vortices will change a little.

#### 4.4. Velocity Distribution in Clearance

Figure 16 shows the velocity contour distribution of the YZ section in the upper crown clearance. Influenced by the rotating wall, the flow velocity from the clearance inlet to the outlet of the labyrinth ring has little difference. After entering the cavity, the flow velocity gradually decreases with the expansion of the flow channel area. Since the UCOS has a certain rotation speed, the flow velocity near the UCOS in the cavity is large. The upper wall is a part of the static top cover of the hydraulic turbine, and the flow velocity near it is small. The low-velocity area in the cavity can be seen through the streamlined distribution to be caused by the vortices. As the runner gradually decreases, the velocity distribution in the upper crown clearance has little difference, but the velocity tends to decrease near the shaft surface.

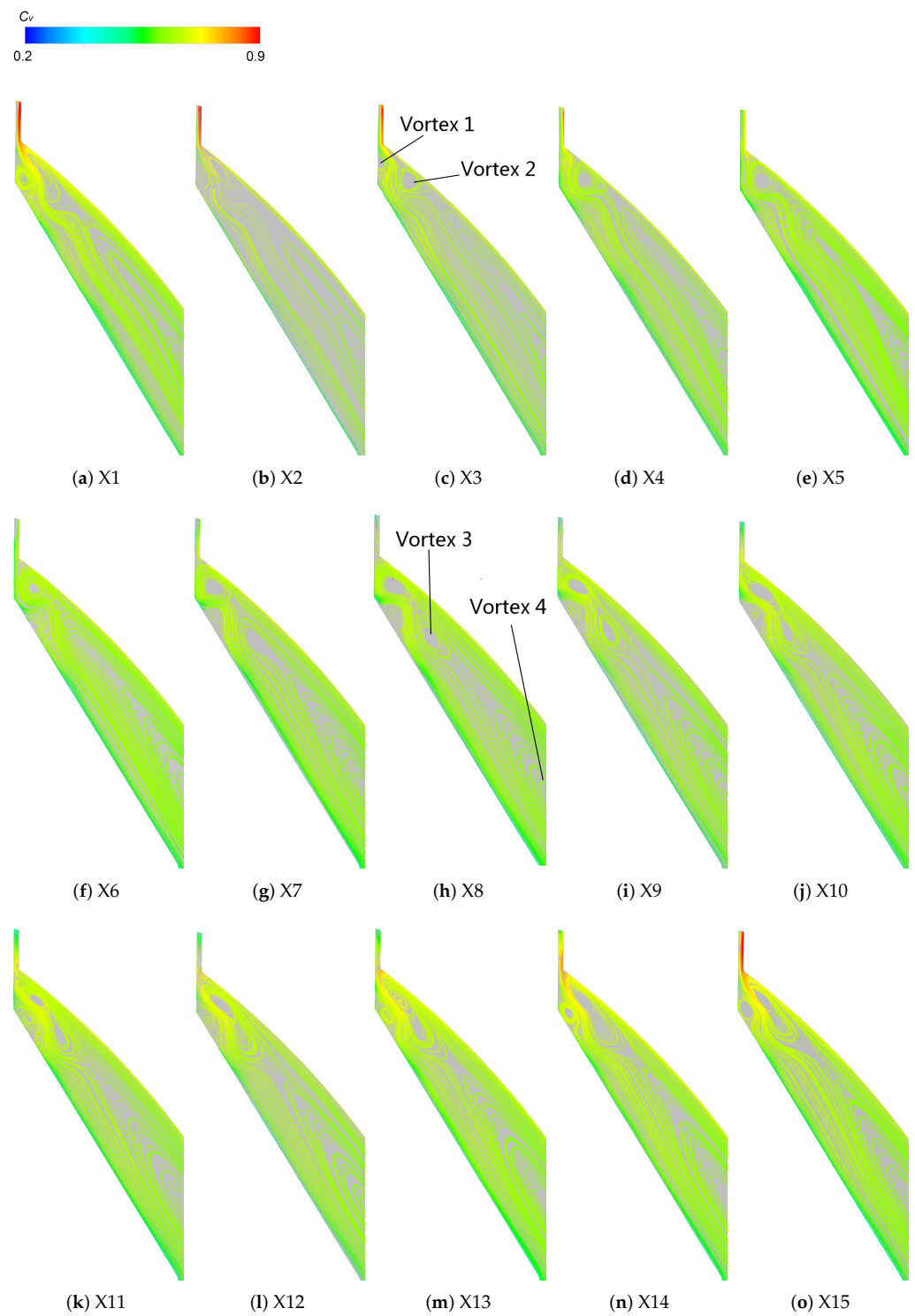
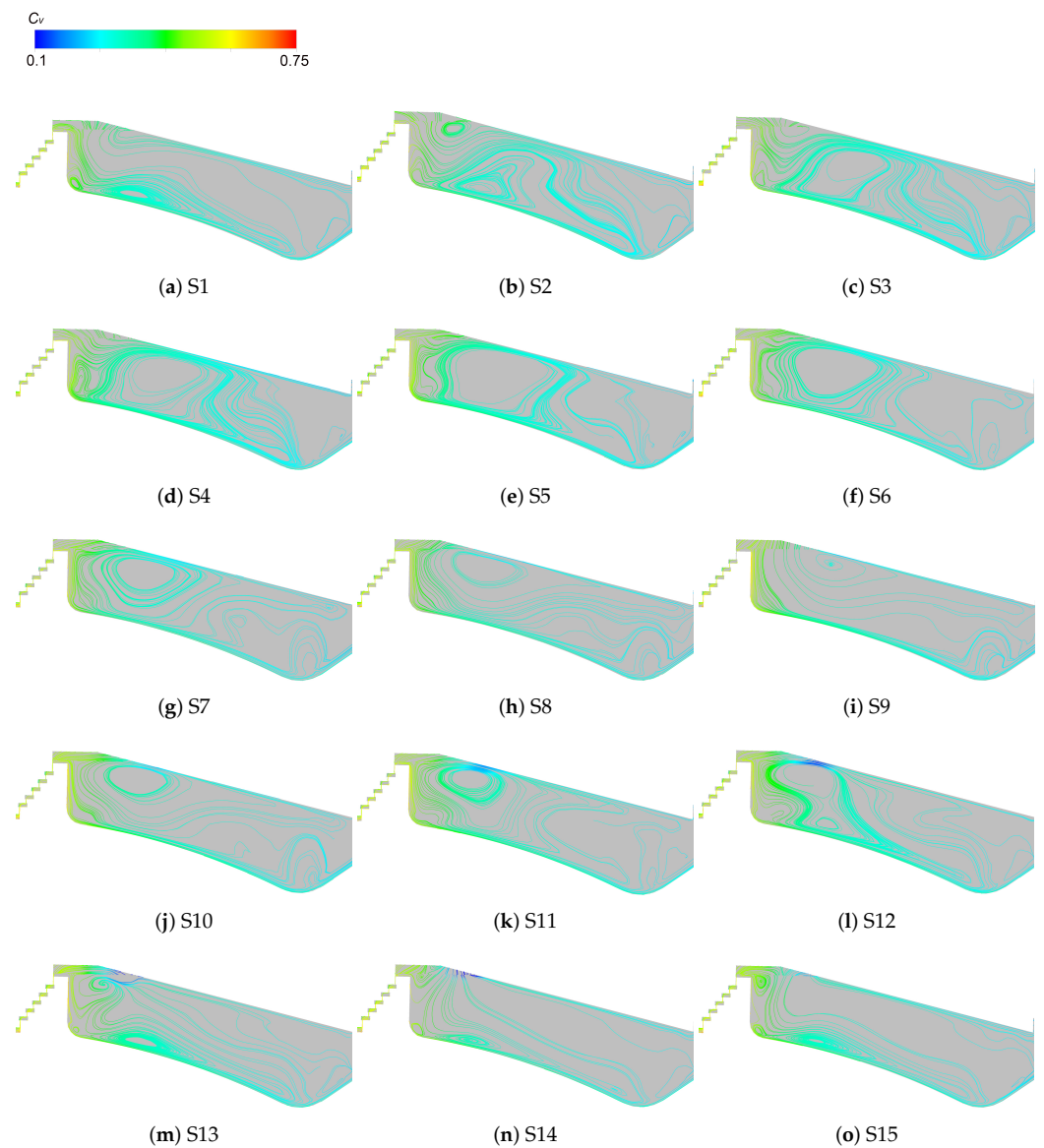
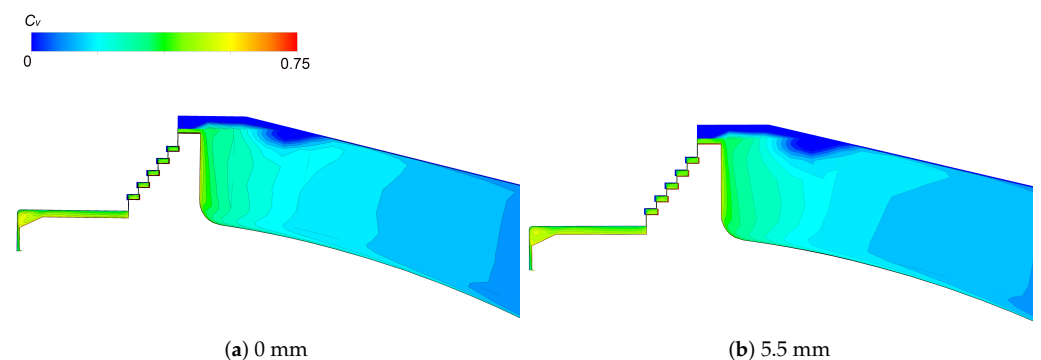


Figure 14. Streamlined distribution of X1–X15 section of runner dropping 0 mm model.



**Figure 15.** Streamlined distribution of S1–S15 section of runner dropping 0 mm model.



**Figure 16.** Velocity distribution of the ZY section of the upper crown clearance.

Figure 17 shows the velocity contour distribution of the YZ section in lower band clearance. There are obvious vortices in the region with higher velocity. Since the LBOS of the lower band clearance has a certain rotation speed, the flow velocity near the rotating wall surface is large. With the runner descending, the velocity distribution law in the lower band clearance does not change significantly, but the speed tends to increase.

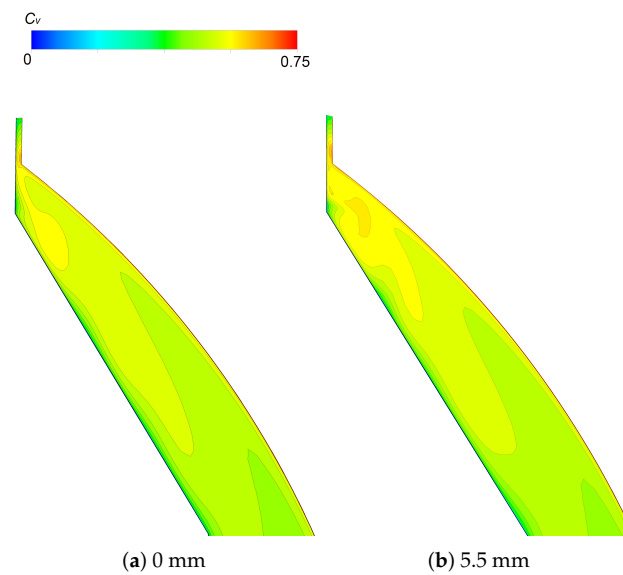


**Figure 17.** Velocity distribution of the ZY section of the lower band clearance.

## 5. Conclusions

As the installation position of the runner decreases, the flow pattern distribution and hydraulic axial force in the runner passage change little. The axial force on the outer surface of the upper crown gradually increases, while the total hydraulic axial force and the hydraulic axial force on the outer surface of the lower band gradually decline. As the runner continues to drop, the axial force will gradually stabilize.

In the upper crown clearance and lower band clearance, the flow near the outer surface of the upper crown and the lower band has a large rotation speed and a large centrifugal force. The flow near the fixed wall rotates at a low speed and has a small rotation speed and a small centrifugal force. The difference between these two forces causes vortices in the cavity, which determines the momentum exchange between water particles with different rotating speeds in the flow field and the friction between the water particles and the fixed wall. Thus, the velocity and pressure distribution are affected, and then the hydraulic force is influenced.

The increase of axial installation dropping of the runner has little effect on the stream-lined distribution of clearance, but the speed and pressure will change. The pressure and velocity in the upper crown cavity will decrease. The velocity at the lower band inlet will increase, and the pressure will decline. The leakage flow of the clearance is also affected to some extent, but it tends to be stable as the dropping distance increases to a certain value.

**Author Contributions:** Conceptualization, Y.L. and C.L.; methodology, C.L.; investigation, C.L. and Y.Z.; validation, X.H. and T.G.; writing—original draft preparation, C.L.; writing—review and editing, C.L. and X.H.; supervision, L.Z. and Z.W. All authors have read and agreed to the published version of the manuscript.

**Funding:** This research received no external funding.

**Institutional Review Board Statement:** Not applicable.

**Informed Consent Statement:** Not applicable.

**Data Availability Statement:** Not applicable.

**Acknowledgments:** The authors received support from the following project: “Research on the mechanism of shaft system dynamic performance change caused by installation deviation of giant hydro-generator units and the engineering applications” from Sinohydro Engineering Bureau 4 Co., Ltd.

**Conflicts of Interest:** The authors declare no conflict of interest.

## Abbreviations

The following abbreviations are used in this manuscript:

|      |  |
|------|--|
| BS   | blade surface                          |
| CFD  | computational fluid dynamics           |
| DCS  | discharge cone surface                 |
| HPUC | horizontal position of the upper crown |
| LBOS | lower band outer surface               |
| LBIS | lower band inner surface               |
| RANS | Reynolds-averaged Navier–Stokes        |
| SST  | shear stress transport                 |
| UCOS | upper crown outer surface              |
| UCIS | upper crown inner surface              |

## References

- Dong, Y.T. Numerical Simulation on the Flow Field of Francis Hydraulic Turbine Runner's Sealing Clearance & the Relief Pipes. Master's Thesis, Xi'an University of Technology, Xi'an, China, 2008.
- Liu, C. Numerical Simulation and the Method of Parametric Mesh Generation of Runner Gap. Master's Thesis, Huazhong University of Science and Technology, Wuhan, China, 2011.
- Lian, J.J.; Qin, L.; He, C.L. Structural Vibration of Hydropower House Based on Prototype Observation. *J. Tianjin Univ. Sci. Technol.* **2006**, *2*, 176–180.
- He, C.L.; Wang, Z.W.; Zhou, L.J. Study on experiment of pressure surge occurs in the draft tube. *J. Mech. Eng.* **2002**, *11*, 62–65. [\[CrossRef\]](#)
- Wang, Z.W.; Zhou, L.J.; He, C.L. Pressure oscillations in a hydraulic turbine draft tube. *J. Tsinghua Univ. Sci. Technol.* **2005**, *45*, 1138–1141.
- Zhou, L.J.; Liu, M.; Wang, Z.W.; Liu, D.M.; Zhao, Y.Z. Numerical simulation of the blade channel vortices in a Francis turbine runner. *Eng. Comput.* **2017**, *34*, 364–376. [\[CrossRef\]](#)
- Trivedi, C. Investigations of compressible turbulent flow in a high-head Francis turbine. *J. Fluids Eng.* **2018**, *140*, 011101. [\[CrossRef\]](#)
- Bucur, D.M.; Dunca, G.; Calinoiu, C. Experimental vibration level analysis of a Francis turbine. In Proceedings of the IOP Conference Series: Earth and Environmental Science, Beijing, China, 19–23 August 2012; Volume 15, p. 062056.
- Wang, F.; Li, X.; Min, Y. Experimental investigation of characteristic frequency in unsteady hydraulic behaviour of a large hydraulic turbine. *J. Hydrodyn. Ser. B* **2009**, *21*, 12–19. [\[CrossRef\]](#)
- Trivedi, C.; Cervantes, M.J. Fluid-structure interactions in Francis turbines: A perspective review. *Renew. Sustain. Energy Rev.* **2017**, *68*, 87–101. [\[CrossRef\]](#)
- Arpe, J.; Nicolet, C.; Avellan, F. Experimental evidence of hydroacoustic pressure waves in a Francis turbine elbow draft tube for low discharge conditions. *J. Fluids Eng.* **2009**, *131*, 081102. [\[CrossRef\]](#)
- Favrel, A.; Müller, A.; Landry, C. Study of the vortex-induced pressure excitation source in a Francis turbine draft tube by particle image velocimetry. *Exp. Fluids* **2015**, *56*, 215. [\[CrossRef\]](#)
- Liu, X.; Luo, Y.; Wang, Z. A review on fatigue damage mechanism in hydro turbines. *Renew. Sustain. Energy Rev.* **2016**, *54*, 1–14. [\[CrossRef\]](#)
- Liang, W.K.; Huang, H.W.; Wu, Z.J. Numerical simulation of fluid-solid coupling of a Francis turbine with an upper crown cavity. *Renewable and Sustainable Energy Reviews. J. Hydraul. Eng.* **2020**, *51*, 1383–1392+1400.
- Sun, H.; Lv, Y.; Ni, J. Effect of seal locations of pump-turbine on axial hydraulic thrust. *J. Mar. Sci. Eng.* **2021**, *9*, 623. [\[CrossRef\]](#)
- Qu, B.X. Analysis and Discussion about Discharging Pipe Structure on Head Cover of Francis Turbine. *Dongfang Electr. Rev.* **2019**, *33*, 71–76.
- Dai, Y.F.; Wang, H.; Zhang, K.W. Research on axial hydraulic thrust of Francis pump-turbine's runner. *J. Hydroelectr. Eng.* **2005**, *24*, 105–109+113.
- Wu, W.X.; Yan, G.J.; Wu, X.R. Analyzing of the axial hydro-thrust test for Francis turbine at different specific speeds. *Large Electr. Mach. Hydraul. Turbine* **2005**, *5*, 40–45.
- Li, H.L.; He, Q.Y.; Zhao, W. Axial Hydraulic Thrust Calculation Method of Francis Pump-Turbine. *Water Resour. Power* **2020**, *38*, 151–155.
- Fu, J.P.; Wan, P.; Duan, K.L. The Prototype Test of Axial Thrust for Unit 6 of Three Gorge Left Bank Hydropower Plant. *Large Electr. Mach. Hydraul. Turbine* **2005**, *5*, 35–39.
- Wu, G.; Zhang, K.W.; Dai, Y.F. Influences of the leakage rate of low specific speed Francis runner on phenomenon of the lifting hydroelectric generator set. *J. Hydroelectr. Eng.* **2004**, *23*, 106–111.
- Liu, D.Y.; You, G.H.; Wang, F. Calculation and analysis of axial thrust acting on turning wheel of flow-mixing reversible hydraulic turbines. *J. Hohai Univ. Nat. Sci.* **2004**, *32*, 557–561.
- Yang, J.D.; Hu, J.H.; Zeng, W. Transient pressure pulsations of prototype Francis pump-turbines. *J. Hydraul. Eng.* **2016**, *47*, 858–864.

24. Ji, X.Y.; Li, X.B.; Su, W.B. On the hydraulic axial thrust of Francis hydro-turbine. *J. Mech. Sci. Technol.* **2016**, *30*, 2029–2035. [[CrossRef](#)]
25. Iliiev, H. Failure analysis of hydro-generator thrust bearing. *Wear* **1999**, *225*, 913–917. [[CrossRef](#)]
26. Ouyang, J.H.; Geng, J.; Xu, L.H. Analysis on strong vibration cause of the powerhouse of a large-scale pumped-storage power station in China and study on its vibration reduction measure. *J. Hydraul. Eng.* **2019**, *50*, 1029–1037.
27. Faria, M.T.C.; Paulino, O.G.; Henrique de Oliveira, F.; Barbosa, B.H.; Martinez, C.B. Influence of mechanical draft tube fish barrier on the hydraulic thrust of small Francis turbines. *J. Hydraul. Eng.* **2010**, *136*, 924–928. [[CrossRef](#)]
28. Kazakov, Y.A.; Pelinskii, A.A. Experimental investigation of the axial force in a submersible, electric well pump. *Chem. Pet. Eng.* **1970**, *6*, 262–263. [[CrossRef](#)]
29. Tao, R.; Xiao, R.F.; Liu, W. Investigation of the flow characteristics in a main nuclear power plant pump with eccentric impeller. *Nucl. Eng. Des.* **2018**, *327*, 70–81. [[CrossRef](#)]
30. Yao, Z.; Zhi, F.L.; Yan, Z.G. Influence Analysis of Lower Labyrinth Pressure Pulsation for Stability of Pumped-storage Unit. *Trans. Chin. Soc. Agric. Mach.* **2014**, *45*, 134–138+110.
31. Xiao, R.F.; Wang, Z.W.; Luo, Y.Y. Dynamic stresses in a Francis turbine runner based on fluid-structure interaction analysis. *Tsinghua Sci. Technol.* **2008**, *13*, 587–592. [[CrossRef](#)]
32. Li, X.; Mao, Z.; Li, W. Prediction and analysis of the axial force of pump-turbine during load-rejection process. In Proceedings of the IOP Conference Series: Earth and Environmental Science, Lausanne, Switzerland, 21–26 March 2020; Volume 440, p. 052081.
33. Zhang, Z. Study on Thrust Support Types of Vertical Axis Hydraulic Turbine Generating Unit. *Large Electr. Mach. Hydraul. Turbine* **2014**, *1*, 52–56.
34. Zhang, Y.; Zheng, X.; Li, J. Experimental study on the vibrational performance and its physical origins of a prototype reversible pump turbine in the pumped hydro energy storage power station. *Renew. Energy* **2019**, *130*, 667–676. [[CrossRef](#)]
35. Mao, Z.; Tao, R.; Bi, H. Numerical study of hydraulic axial force of prototype pump-turbine pump mode's stop with power down. In Proceedings of the IOP Conference Series: Earth and Environmental Science, Lausanne, Switzerland, 8–10 September 2021; Volume 774, p. 012094.
36. Zhou, D.Q.; Chen, Y. Numerical Simulation of Clearance Flow in Francis Turbine with Weep Holes. *Trans. Chin. Soc. Agric. Mach.* **2015**, *46*, 53–58.
37. Lin, W.H.; Mao, Z.Y.; Li, X.Y. Analysis and Improvement of Axial Force on Pump-turbine in Pump Mode. *Trans. Chin. Soc. Agric. Mach.* **2020**, *51*, 132–137.
38. Zhao, L.; Zou, X.Y.; Gong, Z.Y. Effect of Head Cover Decompression Tube Diameter and Guide Vane Rotation Angle on Hydraulic Axial Thrust of A Francis Hydro-turbine. *Water Resour. Power* **2022**, *40*, 188–191+82.
39. Wang, W.Q.; Yin, R.; Yan, Y. Analysis of flow in side chamber and path of comb-labyrinth seal in Francis turbine at different Reynolds numbers. *J. Drain. Irrig. Mach. Eng.* **2014**, *32*, 611–616.
40. Zhou, X.; Shi, C.; Miyagawa, K. Investigation of pressure fluctuation and pulsating hydraulic axial thrust in Francis turbines. *Energies* **2020**, *13*, 1734. [[CrossRef](#)]
41. Muhammad, N.; Alharbi, K.A. OpenFOAM for computational hydrodynamics using finite volume method. *Int. J. Mod. Phys. B* **2023**, *37*, 2350026. [[CrossRef](#)]
42. Muhammad, N.; Lashin, M.M.; Alkhatib, S. Simulation of turbulence flow in OpenFOAM using the large eddy simulation model. *Proc. Inst. Mech. Eng. Part E J. Process. Mech. Eng.* **2022**, *236*, 2252–2265. [[CrossRef](#)]
43. Muhammad, N. Finite volume method for simulation of flowing fluid via OpenFOAM. *Eur. Phys. J. Plus* **2021**, *136*, 1010. [[CrossRef](#)]
44. Muhammad, N.; Ullah, N. Simulation of flow on the hydroelectric power dam spillway via OpenFOAM. *Eur. Phys. J. Plus* **2021**, *136*, 1191. [[CrossRef](#)]
45. Terentiev, L. *The Turbulence Closure Model Based on Linear Anisotropy Invariant Analysis*; Friedrich-Alexander-Universitaet Erlangen-Nuernberg: Erlangen, Germany, 2006.
46. Richardson, L.F. The approximate arithmetical solution by finite differences of physical problems involving differential equations, with an application to the stresses in a masonry dam. *Philos. Trans. R. Soc. Lond. Ser. A Contain. Pap. Math. Phys. Character* **1911**, *210*, 307–357.
47. Richardson, L.F.; Gaunt, J.A. The deferred approach to the limit. *Philos. Trans. R. Soc. Lond. Ser. A Contain. Pap. Math. Phys. Character* **1927**, *226*, 299–361.

**Disclaimer/Publisher's Note:** The statements, opinions and data contained in all publications are solely those of the individual author(s) and contributor(s) and not of MDPI and/or the editor(s). MDPI and/or the editor(s) disclaim responsibility for any injury to people or property resulting from any ideas, methods, instructions or products referred to in the content.